

Electrical impedance tomography methods for miniaturised 3D systems

C. Canali^{1†}, K. Aristovich^{2†}, L. Ceccarelli¹, L. B. Larsen¹, Ø. G. Martinsen^{3,4}, A. Wolff¹, M. Dufva¹, J. Emnéus¹, A. Heiskanen^{1,5}

1. Department of Micro- and Nanotechnology, Technical University of Denmark, 2800, Kgs. Lyngby, Denmark.
 2. Department of Medical Physics and Biomedical Engineering, University College London, Malet Place Engineering Building, Gower Street, London WC1E 6BT, UK
 3. Department of Physics, University of Oslo, P.O. Box 1048, Blindern, 0316 Oslo, Norway
 4. Department of Biomedical and Clinical Engineering, Oslo University Hospital, 0372 Oslo, Norway
 5. E-mail any correspondence to: arto.heiskanen@nanotech.dtu.dk
- † These authors contributed equally to this work.

Abstract

In this study, we explore the potential of electrical impedance tomography (EIT) for miniaturised 3D samples to provide a non-invasive approach for future applications in tissue engineering and 3D cell culturing. We evaluated two different electrode configurations using an array of nine circular chambers (\varnothing 10 mm), each having eight gold plated needle electrodes vertically integrated along the chamber perimeter. As first method, the adjacent electrode configuration was tested solving the computationally simple back-projection algorithm using Comsol Multiphysics in time-difference EIT (t-EIT). Subsequently, a more elaborate method based on the “polar-offset” configuration (having an additional electrode at the centre of the chamber) was evaluated using linear t-EIT and linear weighted frequency-difference EIT (f-EIT). Image reconstruction was done using a customised algorithm that has been previously validated for EIT imaging of neural activity. All the finite element simulations and impedance measurements on test objects leading to image reconstruction utilised an electrolyte having an ionic strength close to physiological solutions. The chosen number of electrodes and consequently number of electrode configurations aimed at maximising the quality of image reconstruction while minimising the number of required measurements. This is significant when designing a technique suitable for tissue engineering applications where time-based monitoring of cellular behaviour in 3D scaffolds is of interest. The performed tests indicated that the method based on the adjacent configuration in combination with the back-projection algorithm was only able to provide image reconstruction when using a test object having a higher conductivity than the background electrolyte. Due to limitations in the mesh quality, the reconstructed image had significant irregularities and the position was slightly shifted toward the perimeter of the chamber. On the other hand, the method based on the polar-offset configuration combined with the customised algorithm proved to be suitable for image reconstruction when using non-conductive and cell-based test objects (down to 1% of the measurement chamber volume), indicating its suitability for future tissue engineering applications with polymeric scaffolds.

Keywords: Electrical impedance tomography, Miniaturised 3D sample, Electrode configurations, Comsol Multiphysics, Customised image reconstruction algorithm

Introduction

Electrical impedance tomography (EIT) is an imaging technique based on multiple impedance measurements

between several electrode couples to map the electrical properties (e.g. conductivity, σ , or permittivity, ϵ) of a sample. Low-amplitude alternating current is injected at a single or a few frequencies and voltages are recorded on the sample surface using the four-terminal method introduced by Schwan in 1963 [1]. This allows impedance measurements with minimised influence of electrode polarisation [2]. EIT involves finding the mathematical solution of the forward and the inverse problem. The forward problem (FP) comprises computation of the potentials at the voltage pick-up (PU) electrodes for a given set of current carrying (CC) electrodes [3]. This allows calculation of the electrical voltage distribution when the injected current and the resistivity distribution within the sample are known. To generate an image, it is necessary to reverse the FP by solving the inverse problem (IP), which involves the calculation of the internal resistivity of the sample based on impedance measurements between the PU electrode pairs.

Both impedance [4] or changes in impedance with time [5] or frequency [6] have been imaged in different fields, spanning from geological studies [7] to medical research [8]. The main advantages of EIT in medicine and biology are non-invasiveness, low cost and good temporal resolution [9,10]. It has been applied for diagnosis of a number of pathological conditions, such as breast cancer [11,12] and stroke [13,14], but also for monitoring brain function [15,16], lung ventilation [17,18] and gastric emptying [19,20]. However, for two main reasons, EIT has not been routinely used in everyday clinical practice, yet [21]. First, EIT has relatively poor spatial resolution (approximately 10% of the image diameter in the cross-sectional plane and 12.5% in the axial plane compared to 1 mm resolution in computed tomography and magnetic resonance imaging [22]), which is further decreased in the regions that are more distant from the electrode array [23]. Secondly, in EIT the IP is ill-posed (i.e. small errors in measurements may cause larger artefacts in the reconstructed image [24]), making the method sensitive to noise. Artefacts may be reduced to produce smoother images by (i) applying regularisation algorithms [25] as well as optimising electrode (ii) number and (iii) configuration [23,26–28].

Although the first medical applications of EIT were presented thirty years ago on human organs of tens of centimetres in diameter [29], only a few in vitro applications

have so far been developed for monitoring cell cultures. One of these [30] applied a simplified concept of EIT, using a linear microarray of 16 electrodes, to map the migration of cells during epithelial stratification. The cultured cells are adherent on the electrodes, modulating the interface impedance. Rahman et al. [31] used impedance spectroscopy to map in vitro cellular morphology using a circular 2D microelectrode array with 8 peripheral electrodes and a central counter electrode. Sun et al. [32] imaged a multi-nuclear single cell mould *Physarum polycephalum* grown on a 2D chip consisting of 16 equally spaced electrodes at the periphery of a circular cell culture chamber ($\text{\O} 6 \text{ mm}$). Meir and Rubinsky [33] presented a preliminary mathematical model for EIT imaging of a single electroporated cell using simulated data. These studies have opened up new interesting perspectives for EIT monitoring of miniaturised 2D cell cultures. However, none of these studies applies the more conventional EIT approach, which is performed on 3D samples, a concept that may find application in monitoring of the overall process of tissue engineering, including scaffold characterisation and 3D cell culture. Recently, Lee et al. [34] optimised new electrode configurations and a customised algorithm based on the back-projection approach that can be potentially used for monitoring 3D tissue cultures. These were tested using a 3D agar scaffold with test objects placed in a cuboidal measurement chamber ($2.4 \times 4.8 \times 2.4 \text{ cm}^3$). Additionally, the performed numerical simulations showed the possibility for further miniaturisation of the setup.

In this work, we investigate the potential of electrical impedance tomography (EIT) to study miniaturised 3D samples using time-difference (t-EIT) and frequency-difference EIT (f-EIT) for potential applications in tissue engineering and 3D cell culturing. Two alternative EIT methods have been validated using an array platform with nine miniaturised circular chambers ($\text{\O} 10 \text{ mm}$). Each chamber comprised eight gold (Au) plated needle electrodes vertically integrated along its perimeter. We analysed the fidelity of image reconstruction by performing impedance measurements on test objects using two alternative electrode configurations and two different image reconstruction methods: (i) the “adjacent” configuration [27,32] in combination with the back-projection algorithm [35] and (ii) the “polar-offset” configuration (a variant of the “polar” configuration [26]) in combination with a customised algorithm previously validated for neural activity imaging by Aristovich et al. [36] The performance of the first method, having technical and computational simplicity, was tested in t-EIT to evaluate its potential for image reconstruction in a miniaturised setup using Comsol Multiphysics. As an alternative method, the polar-offset configuration, which required an additional electrode at the centre of each chamber (8+1 electrodes), was applied together with the customised algorithm using both t-EIT and f-EIT. Linear t-EIT and linear weighted f-EIT [37] approaches were

employed using Gauss-Newton single step linearization with Zeroth order Tikhonov regularisation and subsequent noise-based coefficient of variance correction. The two alternative image reconstruction methods were tested in order to find the most suitable solution for miniaturised 3D setups using a minimal number of electrodes, and hence number of measurements. This is crucial when monitoring tissue engineering processes (e.g. cell growth in scaffolds), where the formation of tissue constructs needs to be followed over time.

2. Material and methods

2.1 Electrodes and instrumentation

Cloud Dragon disposable acupuncture needles ($\text{\O} 0.4 \text{ mm}$ and Au plated) and platinum (Pt) wire ($\text{\O} 0.4 \text{ mm}$) were purchased from PD Vertriebs GmbH (Burgwedel, Germany) and Advent Technologies (East Hartford, UK), respectively. For the impedance measurements, the needles (serving as electrodes) were connected to a Solartron SI1260 + SI1294 impedance analyser (Solartron Instruments, Hampshire, UK) through a Keithley 7001/7012S multiplexer (Solon, Ohio, OH, USA).

2.2 Fabrication of the measurement chamber array

An array of nine circular chambers (10 mm in diameter and height) for parallel analysis was micromilled in poly(methyl methacrylate). Two alternative electrode configurations were tested: (i) the adjacent configuration [27,32], placing 8 Au plated needle electrodes ($\text{\O} 0.4 \text{ mm}$, length 10 mm) equally spaced at the periphery of each measurement chamber, and (ii) the polar-offset configuration (a variant of the “polar configuration” [26]), in which an additional Pt electrode ($\text{\O} 0.4 \text{ mm}$, length 4 mm) was introduced at the bottom centre of each chamber (8+1 electrodes). The Au electrodes fit in eight circular holes ($\text{\O} 0.5 \text{ mm}$, 1 mm deep) drilled at the bottom of each measurement chamber to lock them in vertical position (Fig.1a,b). The Pt electrode was inserted through a central opening ($\text{\O} 0.5 \text{ mm}$) in the bottom plate and sealed with bio-compatible epoxy glue (EPO-TEK[®] 301-2, Lindberg ChemTech AB, Kista, Sweden) (Fig. 1c). The platform lid had openings in different positions for placement of (i) the Au electrodes and (ii) the phantoms with different diameters (1, 2, 3 mm). Crocodile clips were used for connecting the electrodes to the multiplexer/impedance analyser. Pt was cleaned for 10 min in acetone followed by rinsing with Milli-Q water (Millipore Corporation, Billerica, MA, USA) and potential cycling in 0.1 M H_2SO_4 (-0.4 to 1.7 V vs. Ag/AgCl (3M KCl)); approximately 40 cycles at a scan rate of 200 mV/s).

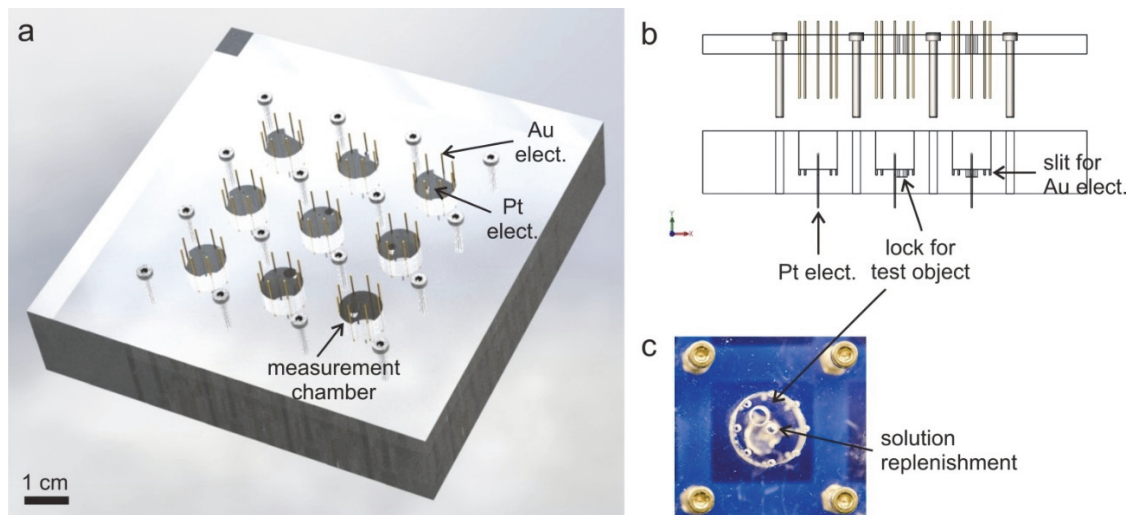


Fig. 1 (a): The measurement chamber array. Eight Au plated electrodes were placed at the periphery of each chamber. When present, the Pt electrode was placed at the centre of the chamber through the bottom plate (8+1 electrodes). (b) Schematic (side view) showing the Pt electrode, the circular slits for positioning the Au electrodes and micromilled depressions at the bottom of the chamber to keep the Au electrodes and the test object in position. (c) Photo of a measurement chamber. The lid had an opening to lock the test object in position and a smaller opening for solution replenishment

2.3 EIT using the adjacent configuration and the back-projection algorithm for image reconstruction

A 0.5 mA AC current was injected in the frequency range between 10 and 100 kHz (10 points/decade) using the adjacent configuration shown in Fig. 2a. Phantom experiments were performed using a cylindrical stainless steel object (\varnothing 2 mm, height 10 mm, $\sigma = 1.7 \times 10^6$ S/m and $\epsilon_r = 1$) placed inside the measurement chamber filled with a conductivity standard solution ($\sigma = 1.3$ S/m and $\epsilon_r = 80$, Hanna Instruments, Kungsbacka, Sweden). Time-difference EIT (t-EIT) was performed by using impedance modulus (evaluated at 5 kHz) before (duplicate) and after the addition of the test object.

The finite element method (FEM) was used to compute the FP and solve the IP using Comsol Multiphysics v.4.4 (AC/DC module). The measurement chamber and its content (electrolyte plus test object for the FP and the plain electrolyte for the IP) was spatially discretised using a tetrahedral mesh and Maxwell equations were solved in matrix form for all mesh elements [38]. This process was repeated for all CC electrode pair combinations. Voltages on the PU electrodes were simulated using the method previously described by Pettersen and Høgetveit [39]. This allowed for the construction of the sensitivity matrix that relates the changes in conductivity in each mesh element to changes in voltage on the PU electrodes [40,41], which form the basic operation for the FP. Once the sensitivity matrix was generated, the effect of each mesh element's (or voxel) conductivity on the total voltage could be obtained by mathematically inverting the matrix. This is the IP, which is ill-posed and requires additional regularisation based on known parameters of the system (e.g. injected current, electrode and electrolyte conductivity).

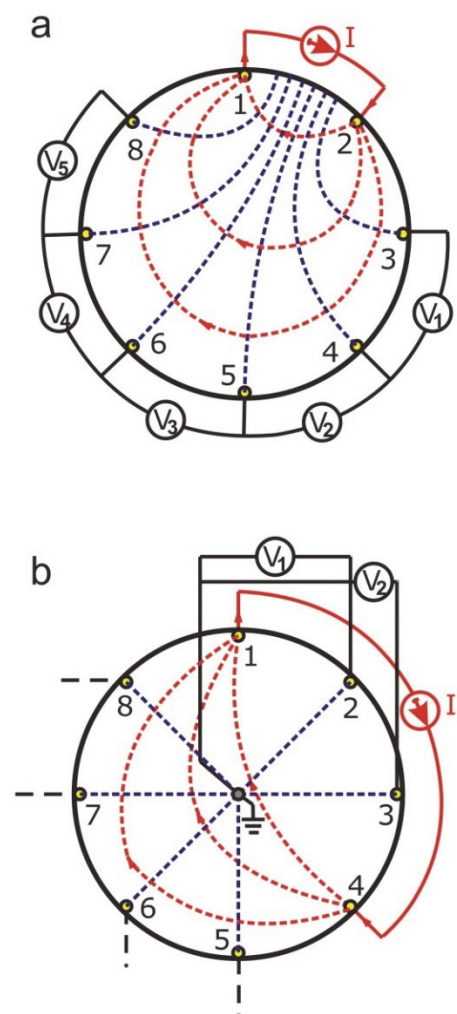


Fig. 2: Schematics of the adjacent (a) and polar-offset (b) configurations. Red and blue dashed lines represent the directions of CC and PU electric fields, respectively. A detailed description of the configurations is given in Supplementary Material S1.

The back-projection algorithm assumes that the optimal solutions are obtained from the values that minimise the difference between the measured and predicted voltages. In addition, it assumes that the conductivity change is uniform in the areas between equipotential lines. Predicted voltages can be obtained by solving the FP. In the IP, the resistivity of each mesh element was weighted by a factor accounting for: (i) the current path between any CC-PU electrode pair, and (ii) the difference between the mesh elements size [42]. The current path was mathematically related to the impedance measurement sensitivity distribution and found by solving the FP. The difference between the voxel size is due to the fact that the mesh is denser in the proximity of the electrodes. For both the FP and the IP, the mesh was generated using Simulink. It consisted of 86978 elements (average element quality of 0.6555) for the FP and 97525 elements (average element quality of 0.7079) for the IP.

2.4 EIT using the polar-offset configuration and a customised algorithm for image reconstruction

A 0.5 mA AC current was injected in the frequency range between 10 and 100 kHz (6 points/decade) using the polar-offset configuration shown in Fig. 2b (8+1 electrodes). Impedance measurements were first made using cylindrical plastic objects of increasing diameter (1 – 3 mm, height 10 mm) placed inside the measurement chamber filled with the electrolyte. t-EIT was performed using impedance data acquired at each frequency before (duplicate) and after the addition of the phantom. Furthermore, two potato test objects were carved to obtain irregular triangular and square 3D shapes (side ~ 2 mm, height 10 mm) to test the accuracy of the algorithm for shape reconstruction of miniaturised objects. The potato objects were placed in two different positions inside the measurement chamber filled with the electrolyte. t-EIT results were compared with those obtained with frequency-difference EIT (f-EIT) between 10 kHz and 100 kHz.

For both t-EIT and f-EIT, the solution of the IP for image reconstruction was done using the customised algorithm developed by Aristovich et al. [36] for neural activity imaging. The reconstruction method used linear single step Gauss-Newton approach (time difference and weighted frequency difference) with a Zeroth order Tikhonov regularisation [43] and subsequent coefficient-of-variance representation (z-score) with respect to the background noise. The algorithm is based on the assumptions that the conductivity change is small and all pixels are equivalent in terms of noise contribution to the resulting conductivity image. Random Gaussian noise with standard deviation determined from the baseline experimental data was used to estimate the response of each pixel to the applied noise. Then, the conductivity change in each pixel of the reconstructed image was divided by the standard deviation of conductivity background noise in order to compute z-score for each pixel.

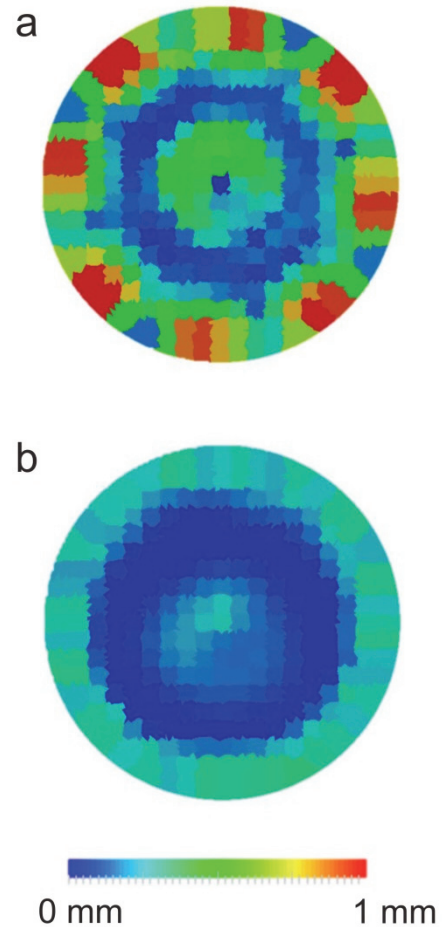


Fig. 3: Computer simulations of the positional accuracy of the customised method using (a) 8+1 and (b) 32+1 electrodes. The positional accuracy (colour bar) for each perturbation location was computed as the distance (in mm) between the centre of the true and reconstructed object, displayed at the true perturbation location.

The z-score, representing the ratio between the signal in the pixel and the background noise, i.e. the conductivity contrast, was used for image reconstruction throughout the 3D geometry.

The positional accuracy of the method was further investigated using 8+1, or 32+1 electrodes for reconstructing a sphere (\varnothing 1 mm) placed in 1200 evenly spaced positions throughout the measurement chamber. A conductivity difference of 10% was given between the sphere and the surrounding electrolyte. A white Gaussian noise of 10 μ V was added to the simulated voltages before reconstruction. The positional accuracy was displayed in terms of the error (difference between the true and the reconstructed sphere centre in mm).

3. Results and discussion

3.1 Choice of electrode number and configuration

Image quality in EIT has been shown to be highly dependent on the number of used electrodes [44]. An increase in the electrode number consequently increases the number of

independent impedance measurements, which should provide more information for image reconstruction [45]. Unlike in most conventional EIT applications, where the electrodes are placed around the sample on its surface, in a miniaturised setup the needle electrodes are placed inside a measurement chamber. In our measurement chamber with 8 electrodes, their total occupied volume is $\sim 1.3\%$ of the chamber volume. If the number of the electrodes is increased beyond 8, the total occupied volume will also significantly increase. Consequently, the shunting effect [38] and polarisation impedance [46] of the electrodes can more significantly influence the measured impedance. The shunting effect is caused by the fact that the electrodes provide a low-resistance path for the current. This comprises both electrodes that are used for a certain measurement and all the other electrodes present in the measurement chamber. Furthermore, although 4T impedance measurements are theoretically free from the influence of polarisation impedance, the injection of current can cause, however, polarisation impedance. Therefore, the impedance measurements forming the basis for the solution of the IP introduce artefacts in the reconstructed image [47]. Polarisation impedance variations that are about 20% or slightly less do not allow meaningful reconstruction of images [48]. One possibility to reduce the influence of polarisation impedance is to employ platinised Pt electrodes [49].

Our work aims at developing an EIT technique relevant for future tissue engineering applications where time-based monitoring of cellular behaviour in miniaturised 3D scaffolds is of interest. Due to this, it is important to evaluate the smallest number of electrodes allowing reconstruction of images with an acceptable quality. Two alternative methods were tested. We used 8 electrodes for the adjacent configuration and 8+1 electrodes for the polar-offset configuration, which are suitably spaced considering the dimension of the measurement chamber. To evaluate the improvement in image quality by using a larger number of electrodes, we performed computer simulations using either 8+1 or 32+1 electrodes for reconstructing a 1 mm sphere placed in 1200 evenly spaced positions throughout the measurement chamber. The accuracy map (Fig. 3) shows that the increased number of electrodes provides an improvement in the positional accuracy for the reconstructed image (< 0.5 mm). However, considering a miniaturised setup, placement of more than 8 electrodes in the periphery of the chamber is not feasible. Moreover, in tissue engineering applications, requiring time-based monitoring of cellular behaviour in a scaffold, also the number of measurements has to be minimised. When using 8+1 electrodes, the measurement matrix comprises 48 measurements, whereas in the case of 32+1 electrodes it would consequently have 960 measurements.

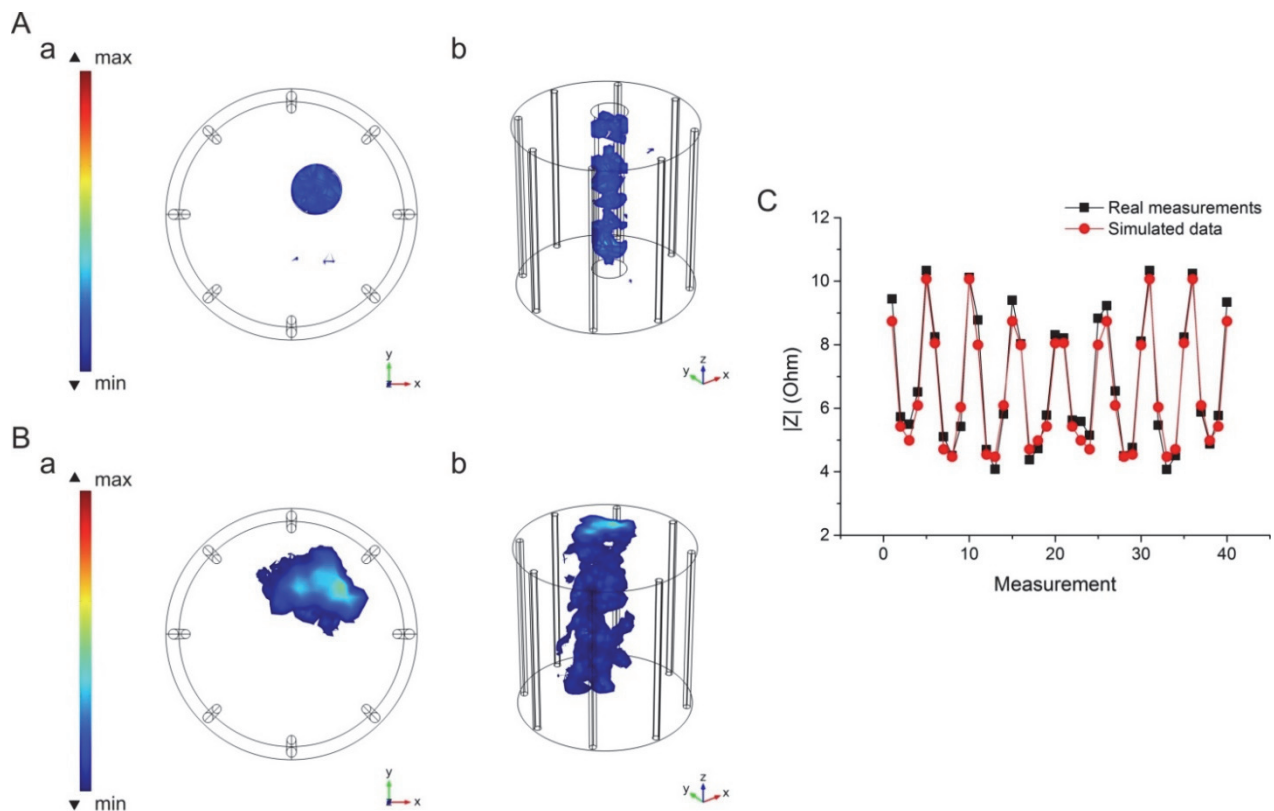


Fig. 4: t-EIT using the adjacent configuration (Fig. 2a) and the back-projection algorithm (Comsol Multiphysics) for image reconstruction of a cylindrical stainless steel object placed in the measurement chamber filled with electrolyte. (A) Computation of the FP (a, top view and b, isometric view). (B) Solution of the IP (a, top view and b, isometric view). The colour scales give a qualitative representation of the object impedance. (C) Match between the impedance measurements and the simulated data in the FP. The impedance modulus, $|Z|$, is reported for all the 40 measurements.

In the adjacent configuration (Fig. 2a), the current is injected through adjacent electrodes and the voltage is measured sequentially from all the other adjacent electrode pairs. Previous work has shown that using the adjacent configuration, the measured voltage is maximum for the adjacent electrode pairs, whereas for the opposite electrode pairs (located 180° across the chamber) the voltage is only about 2.5% of that value [27]. Using 8 electrodes at the periphery of the measurement chamber, a matrix of 40 measurements is obtained. This number comprises also redundant reciprocal measurements [50], as EIT uses four-terminal impedance measurements, for which the principle of reciprocity is valid. According to reciprocity, the measured impedance does not change if the CC and PU electrodes are swapped [50], leading to a matrix of 20 unique measurements when using the adjacent configuration. If a larger number of electrodes were used in the adjacent configuration, this would mainly increase the image resolution at the periphery of the chamber and only to a lesser extent towards the centre. This can be improved, however, by using the polar-offset configuration, which is a variant of the polar (or opposite) configuration [26]. Here, the current is injected through two almost diametrically opposed electrodes (electrodes 1 and 4 in Fig. 2b). The Pt electrode at the centre of the measurements chamber is used as ground for all PU couples employed in the voltage measurements, which increases the image resolution towards the centre of the chamber. Voltage is measured from all other electrodes except the CC couple, resulting in a matrix of 48 measurements as mentioned above. These also comprise redundant reciprocal measurements.

3.2. EIT using the adjacent configuration and the back-projection algorithm for image reconstruction

The adjacent configuration (Fig. 2a) in combination with the back-projection algorithm offers technical and computational simplicity, allowing usage of a commercially available software package, such as Comsol Multiphysics, which minimises the requirement of programming in constructing an algorithm. Moreover, since this method is based on the placement of electrodes only in the periphery of a chamber, it is suitable for applications that utilise a scaffold occupying a considerable volume and cannot be perforated with a central electrode. Fig. 4Aa,b and Fig. 4Ba,b show the computation of the FP and the solution of the IP, respectively, in t-EIT when a cylindrical stainless steel object (\varnothing 2 mm, height 10 mm) was placed in the measurement chamber filled with electrolyte. Impedance measurements were performed in the range of 10 Hz – 100 kHz. 5 kHz was chosen as the frequency for image reconstruction, providing the best match between measured impedance and simulated data. The impedance modulus was used for image reconstruction since impedance measurements showed small absolute values for phase angle ($\sim 1^\circ$ for

electrode pairs far away from the metal object and $\sim 20^\circ$ for electrode pairs close to the object). This indicated low influence from stray capacitance, which is usually the main source of error due to instrumentation.

The quality of the reconstructed image strictly depends on the mesh quality, which can be optimised but not customised when using a commercial software package. The equations integrated in such programs provide less degree of freedom in performing image regularisation. Furthermore, statistical analysis of positional accuracy is not possible. However, the results shown in Fig. 4A and B indicate that the back-projection algorithm and adjacent configuration can provide a qualitatively accurate object position, although showing mesh inhomogeneities, which may be alleviated by integrating a free-form custom mesh. Furthermore, the simulated impedance data (obtained from the solution of the FP) and the impedance measurements (used for solving the IP) are well superimposed, as shown in Fig. 4C and Supplementary Material S2. Previously, we have experimentally shown that the relative variation of impedance is greater when using a conductive test object in comparison with a non-conductive plastic object [51]. This causes a significant limitation when applying the adjacent configuration especially for small objects, due to which it is primarily suitable for image reconstruction of conductive objects. Despite the apparent limitation, the adjacent configuration in combination with the back-projection algorithm may allow t-EIT in applications using conductive 3D scaffolds for cardiac and nerve tissue engineering [52,53].

3.3. EIT using the polar-offset configuration and a customised algorithm for image reconstruction

The electrode arrangement used in the polar configuration [26] provides a more uniform current distribution and better central (but not peripheral) sensitivity compared to the adjacent configuration, which tends to focus on reconstructing peripheral regions of a sample rather than central regions. Moreover, offset methods have been shown to have better performance in comparison with the adjacent configuration [54,55]. When using a small number of electrodes, the polar-offset configuration applied here can more effectively map the entire chamber volume in comparison with the polar configuration originally proposed by Adler et al. [26]. We used a customised algorithm previously validated for EIT imaging of neural activity [36]. Fig. 5 shows t-EIT image reconstruction of cylindrical plastic objects of increasing diameter (1 – 3 mm) placed in the measurement chamber filled with electrolyte. The analysis was performed at each measured frequency between 10 Hz and 100 kHz with almost identical results (difference between all images was $< 0.1\%$). A plastic test object can mimic the dielectric properties of biological cells and tissues [56]. In the case of a 1 mm object, (Fig. 5a), the size of the artefacts on the edge of the chamber are twice as large as the object.

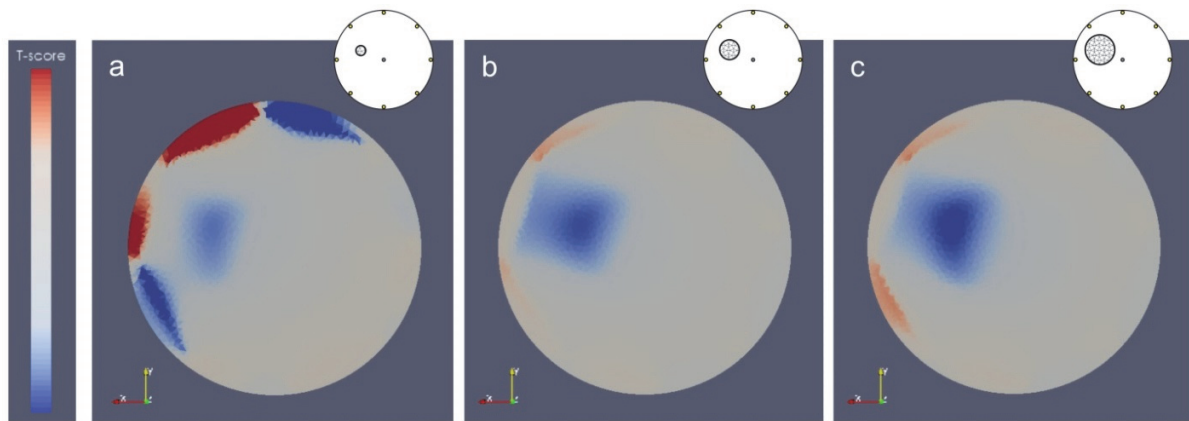


Fig. 5: Image reconstruction (top view) in t-EIT for a cylindrical plastic object placed in the measurement chamber filled with electrolyte using the polar-offset configuration (Fig. 2b) and the customised algorithm. The real position is shown in the schematics at the top (centre-to-centre distance between the object and the chamber: 2.5 mm, angle: 112.5°). Image reconstruction of (a) 1 mm, (b) 2 mm; and (c) 3 mm phantom. The colour scale is in arbitrary units (from -1 in blue, to +1 in red) representing the T-score.

Minor artefacts appear also with 2 and 3 mm objects (Fig. 5b-c). These artefacts may be due to errors in positioning of the central Pt electrode in relation to the peripheral electrodes, which has a more pronounced effect when using a smaller number of electrodes (8+1) for imaging a small object (1% of the measurement chamber volume). Based on the feasibility study using plastic objects, we performed further experiments using irregular triangular and square shaped potato objects (side ~ 2 mm, height 10 mm). Previous studies have shown that potato gives a higher conductivity

contrast against the electrolyte filling the measurement chamber compared to other vegetables (e.g., a carrot) in the frequency range 10 Hz – 100 kHz [14]. Fig. 6Aa and 6Ba show t-EIT image reconstruction for the potato objects. Artefacts on the periphery of the chamber appear slightly pronounced if compared to the 2 mm plastic phantom. This may be due to the fact that potato provides lower conductivity contrast against the electrolyte than plastic. The same reason may also explain the lack of sharpness at the edges of the reconstructed image of the test object.

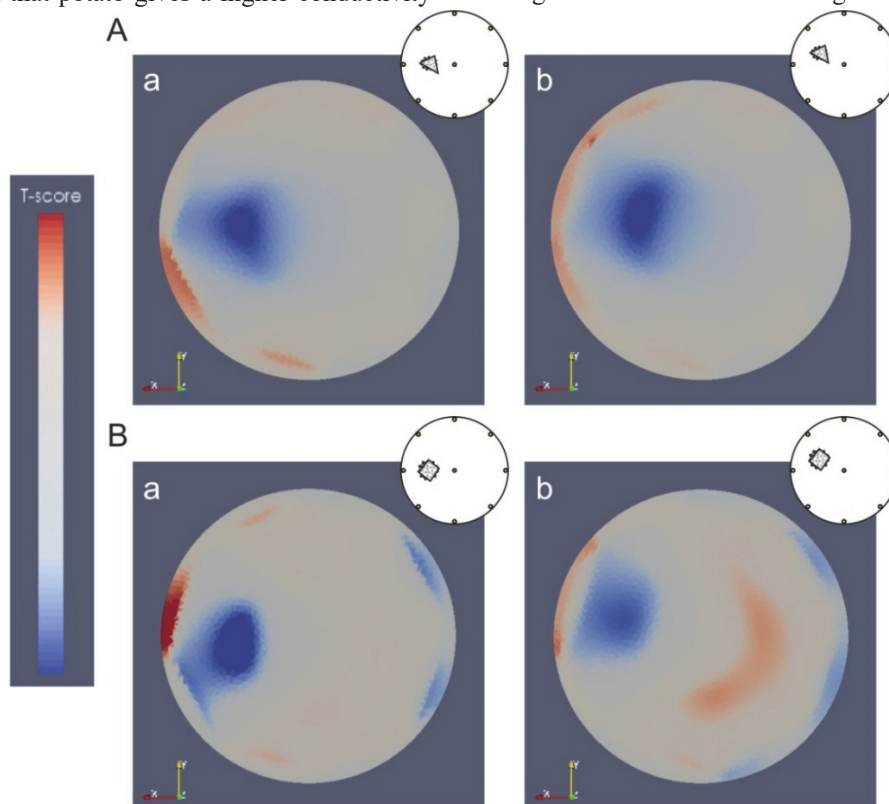


Fig. 6 Image reconstruction in (Aa and Ba) t-EIT and (Ab and Bb) f-EIT for an irregular triangular and square shaped potato object placed in the measurement chamber filled with electrolyte using the polar-offset configuration (Fig. 2b) and the customised algorithm (top view). The real position is shown in the inserts at the top right. Images for a (A) triangular object and (B) square shaped object in two alternative positions: 2.5 mm radial centre-to-centre distance between the phantom and the chamber, (a) angle of 135° and (b) angle of 112.5°. The colour scale is in arbitrary units (from -1 in blue, to +1 in red) representing the T-score.

Potato releases starch in the surrounding medium over time, which may change the conductivity of the electrolyte in the region surrounding the object, additionally contributing to the inaccuracy in the image.

As different biological tissues have different spectral properties, f-EIT gives the advantage that complex tissues, composed of, e.g., fat and muscle, may be characterised more accurately than when using t-EIT. However, f-EIT is more prone to errors than t-EIT since it is based on subtraction of conductivity values taken at two different frequencies. Fig. 6Ab and 6Bb show the reconstructed images using f-EIT.

In terms of the accuracy of reconstructing the test object position, the result is comparable to the one obtained using t-EIT. A potato object is a homogeneous tissue, which may be expected to give a similar result in terms of object shape when using both t-EIT and f-EIT. However, the results obtained using f-EIT show lower accuracy for the reconstructed image. One plausible explanation may be the homogeneity of potato, i.e. the response at different frequencies is similar, which may increase the sensitivity to artefacts. Additionally, the release of starch in the surrounding medium, as explained above, may also contribute to a greater manifestation of artefacts when using f-EIT for imaging a homogeneous tissue.

4. Conclusions

We have presented time-difference and frequency-difference electrical impedance tomography (t-EIT and f-EIT) for imaging miniaturised 3D samples using a minimised number of electrodes vertically placed at the periphery of a cylindrical chamber. A computationally simple method based on the adjacent configuration and back-projection algorithm was shown to facilitate t-EIT imaging of a conductive metal test object. A more elaborate method based on the “polar-offset” configuration and a customised algorithm was tested using t-EIT image reconstruction for plastic and potato objects. This approach showed capability for imaging objects down to 1% of the measurement chamber volume. f-EIT experiments were performed with the same potato objects, indicating the same accuracy in terms of position as shown by t-EIT, albeit with lower image accuracy.

The presented results outline the potentials of the two different EIT methods in miniaturised 3D systems suitable for various tissue engineering applications. The adjacent configuration and back-projection algorithm, which showed applicability for t-EIT imaging of conductive test object, can provide a simple method for faster screening of cell behaviour in conductive scaffolds for, e.g., cardiac and neural tissue engineering. The “polar-offset” configuration and a customised algorithm, sensitive to non-conductive objects, can provide a method to monitor tissue engineering processes in more conventional polymeric scaffolds loaded with cells. Considering the heterogeneity of such cell loaded scaffolds, f-EIT may provide better images due to differential frequency-dependence between the scaffold

material and cells. However, as f-EIT can only be approximated to a linear mathematical problem for impedance contrasts less than 20%, which is usually exceeded in any physiological sample, our f-EIT approach needs to be validated for monitoring of actual tissue engineering processes. On the other hand, for imaging the process of scaffold biodegradation, analogous to the behaviour of starch-leaking potato phantoms, t-EIT may be a more suitable solution.

Acknowledgements

This study and the Ph.D. fellowship of C. Canali were financially supported by the EU-funded project NanoBio4Trans (grant no. 304842). The authors gratefully acknowledge Professor David Holder (University College London, UK) for valuable discussions on impedance tomography.

References

1. H. P. Schwan and C. D. Ferris, in 16th Annual conference on engineering in medicine and biology, ed. D. A. Robinson, Baltimore, Maryland, 1963, pp. 84–85.
2. B. H. Brown, *J. Med. Eng. Technol.*, 2003, 27, 97–108. <https://doi.org/10.1080/0309190021000059687>
3. J. C. de Munck, T. J. Faes and R. M. Heethaar, *IEEE Trans. Biomed. Eng.*, 2000, 47, 792–800. <https://doi.org/10.1109/10.844230>
4. P. J. Vauhkonen, M. Vauhkonen, T. Savolainen and J. P. Kaipio, *Dep. Appl. Physics, Univ. Kuopio*, 1992, 0–3.
5. K. Y. Kim, S. I. Kang, M. C. Kim, S. Kim, Y. J. Lee and M. Vauhkonen, *Inverse Probl. Eng.*, 2003, 11, 1–19. <https://doi.org/10.1080/1068276021000014705>
6. Y. Granot, A. Ivorra and B. Rubinsky, *Int. J. Biomed. Imaging*, 2007, 2007. <https://doi.org/10.1155/2007/54798>
7. S. Stefanescu, C. Schlumberger and M. Schlumberger, *J. Phys. le Radium*, 1930, 1, 132–140. <https://doi.org/10.1051/jphysrad:0193000104013200>
8. R. Bayford and A. Tizzard, *Analyst*, 2012, 137, 4635. <https://doi.org/10.1039/c2an35874c>
9. D. Holder, in *Electrical impedance tomography*, Institute of Physics Publishing, Bristol, 1st edn., 2005, pp. 423–449.
10. D. Holder, in *Electrical impedance tomography*, ed. I. of P. Publishing, Bristol, 1st edn., 2005, pp. 127–166.
11. M. S. Campisi, C. Barbre, A. Chola, G. Cunningham and J. Viventi, *IEEE Eng. Med. Biol. Soc.*, 2014, 1131–1134.
12. R. J. Halter, A. Hartov, S. P. Poplack, W. A. Wells, K. M. Rosenkranz, R. J. Barth, P. A. Kaufman and K. D. Paulsen, *IEEE Trans. Med. Imaging*, 2015, 34, 38–48. <https://doi.org/10.1109/TMI.2014.2342719>
13. M. Mhajna and S. Abboud, *Int. j. numer. method. biomed. eng.*, 2012, 28, 72–86. <https://doi.org/10.1002/cnm.1494>
14. B. Packham, H. Koo, a Romsauerova, S. Ahn, a McEwan, S. C. Jun and D. S. Holder, *Physiol. Meas.*, 2012, 33, 767–786. <https://doi.org/10.1088/0967-3334/33/5/767>
15. D. S. Holder, *Brain Topogr.*, 1992, 5, 87–93. <https://doi.org/10.1007/BF01129035>

16. A. P. Bagshaw, A. D. Liston, R. H. Bayford, A. Tizzard, A. P. Gibson, a. T. Tidswell, M. K. Sparkes, H. Dehghani, C. D. Binnie and D. S. Holder, *Neuroimage*, 2003, 20, 752–764. [https://doi.org/10.1016/S1053-8119\(03\)00301-X](https://doi.org/10.1016/S1053-8119(03)00301-X)
17. B. Amm, T. Kao, X. Wang, G. Boverman, J. Sabatini, J. Ashe, J. Newell, S. Member, D. Isaacson and S. Member, *IEEE Eng. Med. Biol. Soc.*, 2014, 6064–6067.
18. H. Reinius, J. B. Borges, F. Fredén, L. Jideus, E. D. L. B. Camargo, M. B. P. Amato, G. Hedenstierna, A. Larsson and F. Lennmyr, *Acta Anaesthesiol. Scand.*, 2015, 59, 354–368. <https://doi.org/10.1111/aas.12455>
19. F. Podczeczek, C. L. Mitchell, J. M. Newton, D. Evans and M. B. Short, *J. Pharm. Pharmacol.*, 2007, 59, 1527–1536. <https://doi.org/10.1211/jpp.59.11.0010>
20. C. T. Soulsby, M. Khela, E. Yazaki, D. F. Evans, E. Hennessy and J. Powell-Tuck, *Clin. Nutr.*, 2006, 25, 671–680. <https://doi.org/10.1016/j.clnu.2005.11.015>
21. R. H. Bayford, *Annu. Rev. Biomed. Eng.*, 2006, 8, 63–91. <https://doi.org/10.1146/annurev.bioeng.8.061505.095716>
22. P. Metherall, D. C. Barber, R. H. Smallwood and B. H. Brown, *Nature*, 1996, 380, 509–512. <https://doi.org/10.1038/380509a0>
23. P. Kauppinen, J. Hyttinen and J. Malmivuo, *Int. J. Bioelectromagn.*, 2006, 7, 344–347.
24. S. Oh and R. Sadleir, in *Proceedings of the COMSOL conference*, Boston, 2007.
25. J. L. L. Queiroz, *J. Phys. Conf. Ser.*, 2012, 407, 012006. <https://doi.org/10.1088/1742-6596/407/1/012006>
26. A. Adler, J. H. Arnold, R. Bayford, A. Borsic, B. Brown, P. Dixon, T. J. C. Faes, I. Frerichs, H. Gagnon, Y. Gärber, B. Grychtol, G. Hahn, W. R. B. Lionheart, A. Malik, R. P. Patterson, J. Stocks, A. Tizzard, N. Weiler and G. K. Wolf, *Physiol. Meas.*, 2009, 30, S35–S55. <https://doi.org/10.1088/0967-3334/30/6/S03>
27. J. Malmivuo and R. Plonsey, in *Bioelectromagnetism - Principles and applications of bioelectric and biomagnetic fields*, Oxford University Press, New York, NY, USA, 1st edn., 1995, pp. 1012–1022. <https://doi.org/10.1093/acprof:oso/9780195058239.001.0001>
28. N. Polydorides and H. McCann, *Meas. Sci. Technol.*, 2002, 13, 1862–1870. <https://doi.org/10.1088/0957-0233/13/12/309>
29. C. C. Barber, B. H. Brown and I. L. Freeston, *Electron. Lett.*, 1983, 19, 933. <https://doi.org/10.1049/el:19830637>
30. P. Linderholm, T. Braschler, J. Vannod, Y. Barrandon, M. Brouard and P. Renaud, *Lab Chip*, 2006, 6, 1155–1162. <https://doi.org/10.1039/b603856e>
31. A. R. A. Rahman, J. Register, G. Vuppala and S. Bhansali, *Physiol. Meas.*, 2008, 29, S227–S239.
32. T. Sun, S. Tsuda, K.-P. Zauner and H. Morgan, *Biosens. Bioelectron.*, 2010, 25, 1109–1115. <https://doi.org/10.1016/j.bios.2009.09.036>
33. A. Meir and B. Rubinsky, *Biomed. Microdevices*, 2014, 16, 427–37. <https://doi.org/10.1007/s10544-014-9845-5>
34. E. J. Lee, H. Wi, A. L. Mcewan, A. Farooq, H. Sohal, E. J. Woo and J. K. Seo, *Biomed. Eng. Online*, 2014, 13, 1–15. <https://doi.org/10.1186/1475-925X-13-1>
35. D. C. Barber, B. H. Brown and N. J. Avis, *Eng. Med. Biol. Soc. 1992 14th Annu. Int. Conf. IEEE*, 1992, 5, 1691–1692.
36. K. Y. Aristovich, G. S. dos Santos, B. C. Packham and D. S. Holder, *Physiol. Meas.*, 2014, 35, 1095–109. <https://doi.org/10.1088/0967-3334/35/6/1095>
37. S. C. Jun, J. Kuen, J. Lee, E. J. Woo, D. Holder and J. K. Seo, *Physiol. Meas.*, 2009, 30, 1087–1099. <https://doi.org/10.1088/0967-3334/30/10/009>
38. E. Somersalo, M. Cheney and D. Isaacson, *SIAM J. Appl. Math.*, 1992, 52, 1023–1040. <https://doi.org/10.1137/0152060>
39. F.-J. Pettersen and J. O. Høgetveit, *J. Electr. Bioimpedance*, 2011, 2, 13–32. <https://doi.org/10.5617/jeb.173>
40. W. Zhang, J. Zhang and G. Llc, in *SEG Technical Program Expanded Abstracts 2011*, Society of Exploration Geophysicists, San Antonio, 2011, pp. 2539–2542. <https://doi.org/10.1190/1.3627719>
41. D. Holder, in *Electrical Impedance Tomography*, Institute of Physics Publishing, London, UK, First Ed., 2005, vol. 1978, pp. 423–449.
42. J. P. Kaipio, V. Kolehmainen, M. Vauhkonen and E. Somersalo, *Inverse Probl.*, 1999, 15, 713–729. <https://doi.org/10.1088/0266-5611/15/3/306>
43. A. N. Tikhonov, A. A. Goncharsky, V. V. Stepanov and A. Yagola, *Numerical methods for the solution of ill-posed problems*, Springer, Berlin, 1st edn., 1995. <https://doi.org/10.1007/978-94-015-8480-7>
44. M. Tang, W. Wang, J. Wheeler, M. McCormick and X. Dong, *Physiol. Meas.*, 2002, 23, 129–140. <https://doi.org/10.1088/0967-3334/23/1/312>
45. D. C. Dobson and F. Santosa, *SIAM J. Appl. Math.*, 1994, 54, 1542–1560. <https://doi.org/10.1137/S0036139992237596>
46. R. Cardu, P. H. W. Leong, C. T. Jin and A. McEwan, *Physiol. Meas.*, 2012, 33, 817–830. <https://doi.org/10.1088/0967-3334/33/5/817>
47. A. Boyle and A. Adler, *Physiol. Meas.*, 2011, 32, 745–54. <https://doi.org/10.1088/0967-3334/32/7/S02>
48. A. McEwan, G. Cusick and D. S. Holder, *Physiol. Meas.*, 2007, 28, S197–S215. <https://doi.org/10.1088/0967-3334/28/7/S15>
49. T. Dowrick, C. Blochet and D. Holder, *Physiol. Meas.*, 2015, 36, 1273–1282. <https://doi.org/10.1088/0967-3334/36/6/1273>
50. J. Malmivuo, in *Journal of Physics: Conference Series*, 2010, vol. 224.
51. C. Canali, C. Mazzoni, L. B. Larsen, A. Heiskanen, Ø. G. Martinsen, A. Wolff, M. Dufva and J. Emneus, *Analyst*, 2015, 140, 6079–6088. <https://doi.org/10.1039/C5AN00987A>
52. H. Baniasadi, A. Ramazani S.A. and S. Mashayekhan, *Int. J. Biol. Macromol.*, 2015, 74, 360–366. <https://doi.org/10.1016/j.ijbiomac.2014.12.014>
53. A. M. Martins, G. Eng, S. G. Caridade, J. F. Mano, R. L. Reis and G. Vunjak-Novakovic, *Biomacromolecules*, 2014, 15, 635–643. <https://doi.org/10.1021/bm401679q>
54. A. Adler, P. O. Gaggero and Y. Maimaitijiang, *Physiol. Meas.*, 2011, 32, 731–744. <https://doi.org/10.1088/0967-3334/32/7/S01>
55. N. J. Avis and D. C. Barber, *Physiol. Meas.*, 1994, 15, A153–A160. <https://doi.org/10.1088/0967-3334/15/2A/020>
56. H. P. Schwan and S. Takashima, *Bull. Inst. Chem. Res. Kyoto Univ.*, 1991, 69, 459–475.